Accepted Manuscript

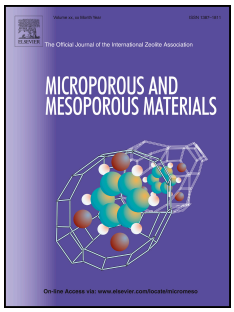

Femto-to nanosecond photodynamics of Nile Red in metal-ion exchanged faujasites

Maria Rosaria di Nunzio, Elena Caballero-Mancebo, Cristina Martín, Boiko Cohen, María Teresa Navarro, Avelino Corma, Abderrazzak Douhal

PII: S1387-1811(17)30547-4

DOI: 10.1016/j.micromeso.2017.08.011

Reference: MICMAT 8498

To appear in: *Microporous and Mesoporous Materials*

Received Date: 20 June 2017

Revised Date: 14 July 2017

Accepted Date: 8 August 2017

Please cite this article as: M.R. di Nunzio, E. Caballero-Mancebo, C. Martín, B. Cohen, Marí.Teresa. Navarro, A. Corma, A. Douhal, Femto-to nanosecond photodynamics of Nile Red in metal-ion exchanged faujasites, *Microporous and Mesoporous Materials* (2017), doi: 10.1016/j.micromeso.2017.08.011.

TOC:

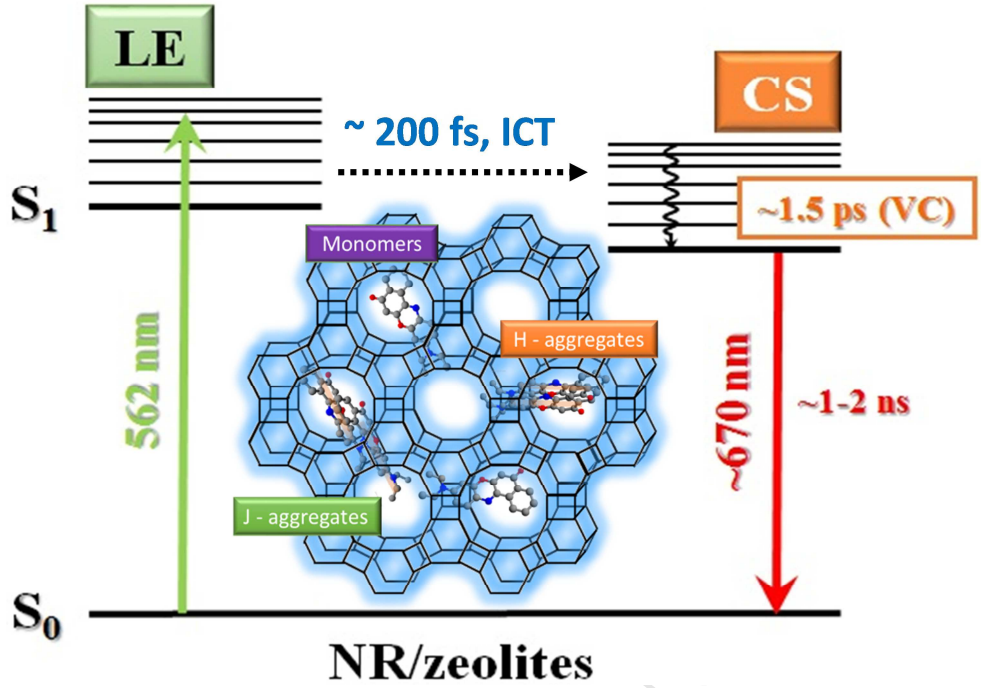

Graphic representation of the different trapped NR populations within the metal-ion exchanged zeolites. The proposed scheme describe their fast and ultrafast photophysical behaviour (LE: Local Excited, ICT: Internal Charge Transfer and CS: Charge Separated State).

Femto- to Nanosecond Photodynamics of Nile Red in Metal-Ion Exchanged Faujasites ≠

Maria Rosaria di Nunzio,[a] Elena Caballero-Mancebo,[a] Cristina Martín,[a,b] Boiko Cohen,[a] María Teresa Navarro,[c] Avelino Corma,[c] and Abderrazzak Douhal*[a]

[a]Departamento de Química Física, Facultad de Ciencias Ambientales y Bioquímica, and INAMOL, Universidad de Castilla-La Mancha, Avenida Carlos III, S/N, 45071 Toledo, Spain.

[b]Chem&Tech – Molecular Imaging and Photonics KU Leuven Celestijnenlaan 200F, B-3001 Leuven, Belgium.

[c]Instituto de Tecnología Química, Universitat Politecnica de Valéncia-Consejo Superior de Investigaciones Científicas (UPV-CSIC), Av. de los Naranjos s/n, 46022 Valencia, Spain.

*corresponding author: Abderrazzak.Douhal@uclm.es

Phone number: +34-925-265717

≠ This work is dedicated to Mía (the daughter of M.R.d.N.)

Abstract

We report on the photodynamics of Nile Red (NR) interacting with faujasite (NaY)-type zeolites having different Na/Al ratios and charge balancing metals (Li^{+}, Mg^{2+}, and Cs^{+}) in dichloromethane (DCM) suspensions. The encapsulation of NR within these materials leads to the formation of different populations, reflected in H- and J-aggregates, monomers, and surface adsorbed species. Due to the interaction of the dye with both the Brønsted and Lewis sites of the zeolite, a bathochromic shift is observed in the steady-state diffuse transmittance and emission spectra. The relative contribution of each population is affected by the Na/Al ratio and the nature of the doping metal ion. These findings are further explored by femto- to nanosecond time-resolved emission experiments, where a multi-exponential behaviour is observed for the excited samples. The fluorescence lifetimes range from ~100 ps to ~2 ns. They are assigned to the emission from H- and J-aggregates and monomers. At low Na/Al ratios, we observe an increase in the fluorescence time constants which is explained in terms of H-bonds formation between NR and the zeolite framework, while the change in the emission lifetimes for the metal ion exchanged zeolites is due to the variation of the properties (size and polarization ability) of the exchange cation. An ultrafast formation (~200 fs) of a charge-separated state (CS) followed by a vibrational cooling (~1-2 ps) are observed in the fluorescence up-conversion transients. These results indicate a strong interaction between NR and the studied zeolites and may help for the design of metal ion sensors and for a better understanding of nanocatalysis.

Keywords: Lewis and Brönsted acidity; H- and J-aggregates; host-guest interaction; Silica-based materials

Introduction

Zeolites have been extensively used as organized media in a wide range of applications, such as heterogeneous catalysts, drying agents, molecular sieves, chemical sensors, and nanocarriers in drug delivery.[1-15]

Zeolites are crystalline, microporous aluminosilicates with open framework structures consisting of channels and cages of discrete nanometric sizes.[16-21] A zeolite is considered a solid acid-base pair, where the protons and the matrix oxygens represent the Brønsted and Lewis sites, respectively.[22] On the other hand, the exchangeable cations interact in a weaker fashion with the anionic lattice through ionic-type bonds. Zeolites aptitude to accept electron pairs make these materials act as Lewis acids.

The chemical properties, including the composition, nature of the cations, and lattice structure, of faujasites can be well tuned. Due to the reduced space and the rich variety of interaction sites within the faujasite framework, these materials are capable of changing and controlling the behaviour of confined organic and inorganic molecules through specific and non-specific host-guest and guest-guest interactions.[23, 24] Thus, the structural features and the physicochemical properties of zeolites can be monitored by the use of specific guest molecules acting as probes through steady-state and transient spectroscopy, in addition to other techniques. In this regard, several studies have demonstrated that the photobehaviours of several encapsulated molecules, such as salicylaldehyde azine (SAA), 1-phenylazo-2-naphthol (Sudan I), 2-(2-hydroxyphenyl)benzoxazole (HBO), or (E)-2-(2-hydroxybenzyliden)amino-4-nitrophenol (HBA-4NP),[25-30] are largely affected by the composition and structure of the host zeolite.

Nile Red (NR, Scheme 1) is one of the best candidates to explore the effect of the zeolite structure composition on the acidic properties of the catalytic sites. NR is a highly polar and hydrogen-bond sensitive fluorescent molecule with strong solvatochromism observed in different solvents.[31-33] The dependence of the NR photobehaviour on the solvent polarity, which has been reported in several experimental and theoretical works, is due to the intramolecular charge-transfer (ICT) character in NR's electronically first singlet excited state.[34-36] This behaviour is a consequence of the presence of electron donor (diethylamino) and electron acceptor (quinoid) moieties in the molecular structure.[37] Due to NR's remarkable sensibility to the

microenvironment, NR has been widely employed to probe the chemical and structural properties of different heterogeneous and/or organized media.[38-54] Recently, the behaviour of NR in the presence of both normal and doped (with Al, Ga, Ti, and Zr) MCM41 mesoporous materials in dichloromethane (DCM) suspensions was reported to be affected at both its ground and excited states by Brønsted (H-bond formation) and Lewis interactions between the dye and the host.[50] Different populations (monomers and H- and J-aggregates) were observed in the steady-state experiments, associated with large bathochromic shifts. The femto- to nanosecond dynamics of the NR/R-MCM41 complexes revealed great complexity compared with the dynamics observed for the free dye in pure DCM. The encapsulation of NR within faujasite zeolites 13X and LZY-82 was previously observed using steady-state and picosecond-time-resolved emission studies.[52]

The obtained results are of interest in the design of metal-ion sensors The $E_T(30)$ values for 13X and LZY-82 zeolites were estimated to be 55.5 ± 1, indicating that the micropolarity of the zeolite environment was similar to that of a 1:1 (v/v) aqueous solution of methanol. However, observation of the dynamics of NR/zeolites complexes on the ultrafast time scale, which may provide more accurate descriptions of these systems, has not been performed.

Herein, we explore the interaction of NR with Na-Y-type zeolites containing different Na/Al ratios and charge-balancing metals in DCM suspensions using steady-state, UV-visible, and time-resolved (femto- to nanosecond) emission spectroscopies. Our aim was to characterize the zeolites and the effects of structural changes on the photophysical behaviour of the probe. The results showed that the interaction with the hosts affects both the ground-(S_0) and excited-(S_1) state properties of NR in terms of the acidities (Brønsted and Lewis) and electrostatic interactions experienced by the dye in contact with the host framework. We observed the formation of different ground-state populations of NR (monomers, H- and J-aggregates, and surface-adsorbed species) whose relative contributions depended on the Na/Al ratio and the nature of the metal ions. These findings were further supported by time-resolved picosecond emission measurements, which revealed multi-exponential behaviours for the studied composites. Femtosecond-fluorescence spectroscopy showed an ultrafast formation (~200 fs) of a charge-separated (CS) state, followed by vibrational cooling in the range of ~1-2 ps. To obtain a more accurate characterization, we compared the dynamics observed here with

those obtained in presence of the MCM41-based mesoporous materials previously reported.[52]

The obtained results are of interest in the design of metal-ion sensors and to understand photocatalytic mechanisms using this type of host materials.

1. Experimental

NR and anhydrous DCM (spectroscopic grade ≥99.8%) were purchased from Sigma-Aldrich and used without further purification. The faujasite zeolites (CBV 500, CBV 300, and CBV 100, Table 1S in the Supporting Information, SI) were all purchased from Zeolyst and used as received. The Li-Y, Mg-Y, and Cs-Y faujasites were obtained by an ion-exchange procedure using CBV 500 as a precursor, and the sample preparation is explained in the SI. Details on the synthesis of the NR/zeolite samples (CBV 500, CBV 300, CBV 100, Li-Y, Mg-Y, and Cs-Y), together with the dye loading efficiencies, are given in Figure 1S and Table 2S.

Steady-state UV-visible absorption and diffuse-transmittance (DT) spectra were recorded on a Jasco V-670 equipped with a 60-mm integrating sphere (ISN-723). Emission spectra were recorded using a Fluoromax-4 (Jobin-Yvone).

Emission lifetimes were measured using a picosecond time-correlated single-photon-counting (TCSPC) spectrophotometer (FluoTime 200, PicoQuant), as previously described.[55] The fluorescence signal, gated at the magic angle (54.7°), was monitored at a 90° angle with respect to the excitation beam at discrete emission wavelengths. The samples were excited by a 40-ps pulsed diode laser centred at 635 nm (< 5 mW, 40 MHz repetition rate). For excitation at 750 nm, we used the output from a pulsed (90 fs, 2.5 W, 80 MHz) Ti:sapphire oscillator (Mai Tai HP, Spectra Physics). In these experiments, the fs laser excitation was set at a very low power to avoid undesired photochemistry. The instrument response function (IRF) was ~70 ps and was measured using a standard LUDOX (Sigma-Aldrich) solution placed in a 1 cm cell. No differences between the measured IRF in the LUDOX solution and pure zeolite suspensions in DCM were observed. The decay data were analysed using the FluoFit software package (PicoQuant). Exponential decay functions were convoluted with an experimental response function and fit to the experimental decay. The shorter component, which was resolved after a convolution process, had a decay time of 15 ps. The quality of the fits as well as the number of exponentials were carefully selected

based on the reduced χ^2 values (which were ≤ 1.1) and the distributions of residuals. For higher values of χ^2, the used exponential function was disregarded, and other components were added to improve the quality of the fit. The estimated uncertainty of the time constants, considering the errors from the experiments as well as those arising from the multi-exponential fit of the signals, was ~20%.

Time-resolved emission decays were collected using a fluorescence up-conversion technique.[28] The system consisted of a femtosecond optical parameter oscillator (Inspire Auto 100) pumped by 820-nm pulses (90 fs, 2.5 W, 80 MHz) from a Ti:sapphire oscillator (MaiTai HP, Spectra Physics) to generate the excitation beam at 562 nm (~15-20 mW). The polarization of the latter was set to the magic angle with respect to the fundamental beam. The sample was placed in a 1-mm-thick rotating cell. The fluorescence was focused with reflective optics into a 0.3-mm β-BaB_2O_4 (BBO) crystal and gated with the fundamental femtosecond beam. The IRF of the apparatus (measured as the Raman signal of the pure solvent) was ~200 fs (full width at half-maximum, FWHM) at the excitation wavelength. To analyse the decays, a multi-exponential function convoluted with the IRF was used to fit the experimental data. In all cases, the errors for the calculated time components were smaller than 15%. All the experiments were performed at room temperature (293 K).

2. Results and Discussion

2.1. Steady-State UV-Visible Absorption and Emission Studies

2.1.1. Steady-State Absorption Measurements of NR Interacting with the CBV and the Metal-Ion-Exchanged M-Y (M = Li^+, Mg^{2+}, Cs^+) Zeolites

To begin, we recorded the steady-state UV-visible spectra of NR upon interaction with the different CBV (different Na/Al ratios) and metal-ion-exchanged M-Y (M = Li^+, Mg^{2+}, Cs^+) zeolites. When preparing the NR/CBV and NR/M-Y composites, upon addition of the zeolite to the DCM solution, we observed an instantaneous colour change of the zeolite powder from white to light green or blue, suggesting an immediate interaction between the dye and the zeolite materials (Inset of Figure 1A). For these composites, we obtained higher loading efficiencies compared to the ones using MCM41 under the same experimental conditions, thus suggesting a stronger interaction of NR with the zeolite cages.[52] This behaviour will be further discussed taking into account the properties of the different mesoporous materials in Section 2.4.

Figure 1 shows the normalized UV-visible DT spectra of NR (2×10^{-5} M) in the presence of (A): (1) CBV 500, (2) CBV 300, and (3) CBV 100 and (B): (1) Li-Y, (2) Mg-Y, and (3) Cs-Y in DCM suspensions, together with the absorption spectrum of the dye dissolved in the same solvent as a reference. For the composite suspensions, the scattered background was removed by subtracting the DT spectra of the unloaded zeolites. In pure DCM, the dye exhibited a broad, structureless band with a maximum absorption intensity at ~537 nm, assigned to the $S_0 \rightarrow S_1$ (π,π^*) transition.[32-36] The large bathochromic shift from ~537 to 598 nm (~1900 cm^{-1}) and the appearance of structured bands for both the NR/CBV and NR/M-Y samples indicate the formation of different NR populations strongly interacting with the host frameworks. As suggested in Figure 1, for all the DCM-dissolved composites, a very small amount of free NR existed in equilibrium with the encapsulated species, but the band of the free dye was not detectable in the DT spectra.

To obtain a better understanding of the origin of these absorption changes, the normalized DT spectra were deconvoluted into their constituting components.

2.1.2. Deconvolution Analysis of the DT Spectra of NR Interacting with the CBV Zeolites

The deconvoluted NR/CBV DT spectra consist of six bands centred at 549, 593, 622-623, 646-651, 679-681, and 734-736 nm with relative contributions to the total spectra (% integral intensities) of 15-22, 25-31, 13-17, 22-2, 4,4-9, and 4-14%, respectively (Figure 2S, panels A, B, and C). The large number of bands required to obtain an accurate fit of the DT spectra reflects the heterogeneity of the samples. The longest dimension of NR (~15 Å, Scheme 1) slightly exceeds that of the faujasite supercage (~13 Å in diameter). Moreover, the short dimension of NR (~6 Å) is also comparable to the diameter of the "windows" interconnecting the cages (7-8 Å). Therefore, NR can diffuse within the inner channels and pores of the hosting zeolite, and the encapsulated species are most likely located between two neighbouring supercages.

Band at 549 nm: this band does not differ considerably from the corresponding band of the free NR in DCM (537 nm), suggesting that the dye is still exposed to the DCM solvation.[34-36] Moreover, the use of more concentrated initial solutions of NR leads to a broadening of the band, together with an increase of the % integral intensity

(Figure 3S and Table 3S). Based on these considerations, we assign this band to NR species weakly interacting with the zeolite framework.

Band at 622-623 nm: next, based on previous reports,[52, 53] we suggest that the band centred at ~620 nm is due to the monomer population interacting with the framework through H bonds, where the acidity (OH groups) of the zeolite leads to a strong interaction with the dye, likely involving the NR carbonyl group.[51-56]

Bands at 593 and 646-651 nm: on the other hand, several studies on NR interacting with silica-based materials have demonstrated dye aggregation.[47-51] Moreover, we recently showed evidence for the formation of H- and J-aggregates of NR within MCM41 mesoporous materials.[52, 53] Aggregation is a common process for many organic molecules even at low concentrations. The limited space provided by the host promotes specific and non-specific interactions between the adsorbed molecules, which may lead to the formation of both H-(face-to-face) and J-(face-to-tail) aggregates.[57-64] Thus, following excitonic theory, we assign the band blueshifted by ~790 cm^{-1} (593 nm) with respect to that of the encapsulated monomers to H-aggregates and assign the band redshifted by ~650 cm^{-1} (~650 nm) to J-aggregates. The observed difference between the emission intensity maxima of the aggregates lies in the different energy levels involved in their electronic transitions. These energies depend on the type of monomer-monomer interaction (charge-charge and dipole-dipole) and on the behaviour of the involved species interacting with the framework. A general rule cannot be used to predict the exact shifts that the spectra of the aggregates will exhibit, due to the intrinsic guest-guest and guest-host interactions in each system. J-aggregate absorptions are characterized by a sharp band, but due to the heterogeneity of the samples, the resulting absorption becomes broader. In this case, several positions and/or orientations that the molecules can assume with respect to the host system lead to a broadened J-aggregate band.

Band at 679-681 nm: Al-rich zeolites show the presence of extraframework (EF) Al-oxide-containing species, which are mostly responsible for the formation of Lewis acidic sites.[65] The structures of six different extraframework aluminium species (Al^{3+}, $Al(OH)^{2+}$, AlO^{+}, $Al(OH)^{2+}$, AlO(OH), and $Al(OH)_3$), which can likely exist and coordinate in zeolites, were recently studied by density functional theory (DFT).[66] All the zeolites studied in the present work were characterized to have small SiO_2/Al_2O_3 mole ratio values (5.1, Table 1S), suggesting the presence of EF species and Lewis

acidity, in addition to Brønsted acidity. Consequently, the formation of a second population of J-type-aggregates (J-aggregates-2, ~680 nm band) in the vicinity of the Al centres is expected,[65] in agreement with previously reported results on NR interacting with Al-doped MCM41 materials.[53]

Band at 734-736 nm: finally, the redshifted band at ~735 nm likely arises from NR species strongly stabilized in specific internal acidic sites of the zeolite. Here, the strong H-bonding ability and the high polarity of the host framework may stabilize the lowest unoccupied molecular orbital (LUMO) energy of the encapsulated dye, thus redshifting the NR absorption. The above assignment is supported by the reduction of the absorption intensity of the redshifted band after washing the NR:zeolite complexes with DCM (as an example, see Figure 1S). The strongly acidic sites of a protonic zeolite can enhance the adsorption of DCM.[67] Therefore, we rationally determine a competition existing between NR and DCM for those acidic sites during the washing procedure. Due to its high strength of interaction with the zeolite, DCM likely replaces most of the adsorbed NR molecules from the inner cavities to the superficial sites of the zeolite.

Now, we turn our attention to comparing the DT spectra of the three NR/CBV composites. We observed different relative contributions to the total DT spectrum of the NR populations in presence of CBV 500, CBV 300, or CBV 100. The percent of weakly interacting NR (band at 550 nm), being 15% for both CBV 500 and CBV 300, increases to 22% for CBV 100. The population of H-aggregates (band at 593 nm) also becomes larger for CBV 100 (the integral intensities increase from 25 to 31% from CBV 500 to CBV 100), while the population of J-aggregates (band at ~650 nm) is nearly unchanged (integral intensity = 24 and 22% for CBV 500 and CBV 100, respectively). Finally, the band at ~735 nm shows the highest intensity in the presence of CBV 500, which is also confirmed from the deconvolution of the DT spectra, where the integral intensity for this band increases from 4 to 14% from CBV 100 to CBV 500.

The obtained results can be understood considering the specific properties of the studied CBV zeolites. First, CBV 500 shows the lowest Na/Al ratio (0.01, Table 1S), and the nominal cation is an ammonium (NH_4^+) ion. On the other hand, CBV 100 solely contains Na^+ as the nominal charge-compensating cation (Na/Al ratio = 1.2). This indicates the presence of extra free Na^+ species in the zeolite framework, which provides to the zeolite an extra electrostatic character.

Finally, CBV 300, also containing NH_4^+ as a nominal cation, is an intermediate case (Na/Al ratio = 0.17, Table 1S). The deamination process of the NH_4Y zeolite occurs in two endothermic steps: 1) desorption of NH_3 from the small pores at 250 °C and 2) desorption of NH_3 from the large pores between 300 and 400 °C (for the definition of the small and large pore structures, *vide infra*).[66] These dissociations lead to the formation of acidic sites within the zeolite framework, which are weaker in the small pores than in the large ones.[68] Thus, we expect that, during the drying process in our experimental procedure (6 h at 480 °C) to prepare the zeolite for mixing with NR in DCM, NH_3 is most likely fully liberated and that protons reside in the framework. As a result, the number of OH groups and thus the acidity of the zeolite increase. Among the studied CBV zeolites, the heating process converts CBV 500 into the most acidic framework, with the smallest amount of Na^+ cations. In the NaY zeolite, the cations are primarily located in sites I (in the hexagonal prism) and I′ (in the sodalite cage, close to the hexagonal window of the hexagonal prism) in the small pore system and in sites II (at the centre of the hexagonal window between the sodalite cage and the supercage) in the large pore system.[69] In presence of a sufficient number of Na^+ cations, such as in CBV 100, sites II are nearly always the preferred site for ion occupation, as this site is nearly always completely populated because the distribution at sites II minimizes the cation-cation repulsions.

The different acidity, Na^+ content, and Na^+ distribution in CBV 500, CBV 300, and CBV 100 should affect the contribution of each NR population. More specifically, the increased contribution from the weakly interacting NR species in the presence of CBV 100 with respect to the case of CBV 500 and CBV 300 is due to the favourable electrostatic interactions of NR with Na^+ cations (sometimes referred to as π-cation interactions), which are most abundant in CBV 100 as its Na/Al ratio is higher than one (1.2). For the NR/CBV500 and NR/CBV300 composites, as their Na/Al ratios are lower than one (0.01 and 0.17, respectively), the electrostatic interactions with the free Na^+ species are supposed to be nearly absent. Moreover, the number of the monomers and H-aggregates increase, and the number of J-aggregates decreases from CBV 500 to CBV 100 due to the reduced number of acidic interaction sites. Remarkably, the smallest number of Na^+ cations in CBV 500 should correspond to the highest number of available sites II. As a result, red-absorbing NR species may be favoured at these

positions. The lower contribution from the J-aggregates-2 for CBV 100 is most likely because of the competition of NR with the Na^+ ions occupying the Al sites.

2.1.3. Deconvolution Analysis of the DT Spectra of NR Interacting with the Metal-Ion-Exchanged M-Y (M = Li^+, Mg^{2+}, Cs^+) Zeolites

When exchanging the cation from Na^+ to Li^+, Mg^{2+}, or Cs^+, several zeolite characteristics change, inducing modifications in the overall adsorption strength and generating defects that increase the acidity of the material.[70] The variation of the cation size, while bearing the same charge, affects both the polarizability and the electrophilicity of the ion. Similar to the NR/CBV samples, the NR/M-Y DT spectra (Figure 2S, panels D, E, and F and Table 3S) are composed of six bands (except for NR/Cs-Y) centred at 549, 593, 622-623, 646-648, 673-679, and 707-735 nm, with contributions to the whole spectra (% integral intensities) of 14-22, 27-30, 18-23, 22-29, 4-7, and ~5%, respectively.

To estimate the effect of metal substitution in the zeolite framework on the steady-state behaviours of the NR:zeolite composites, we will compare the obtained results with those found for NR/CBV 500, as CBV 500 is the precursor for the three synthesized M-Y zeolites. It is worth to mention that the M/Al values are 1, 0.13, and 0.15 for Li-, Mg-Y, and Cs-Y zeolite, respectively, thus excluding the presence of free metal cationic species within the framework.

For the NR/Li-Y sample, the contribution of the weakly interacting NR (22%) is larger than that calculated for NR/CBV 500 (15%), which is due to the higher electron affinity of Li^+ compared to that of Na^+ (EA = 59.6 and 52.9 $kJmol^{-1}$, respectively) and, therefore, due to the stronger electrostatic interactions exerted from the Li^+ cations to the NR molecules. Both the H- and J-aggregates show similar contributions to those in the presence of CBV 500; however, an increase of the monomer population is observed (from 13 to 18% from NR/CBV 500 to NR/Li-Y), in disfavour of the red-absorbing species (%integral intensities = 14 and 5 for NR/CBV 500 and NR/Li-Y, respectively). The increase of the monomer contribution is explained by the smaller size of Li^+ (d = 0.76 Å)[71] compared to that of Na^+ (d = 1.02 Å),[71] thus allowing more space for the guest molecules to interact with the zeolite framework.

For NR/Mg-Y, the contributions from the monomers (622 nm) and both J-type populations slightly increase compared to those for Li-Y, while the H-aggregates show

the same integral intensity value. The observed changes reflect the smaller size of Mg^{2+} (d = 0.72 Å)[71] compared to the other ions, which provides more available space to accommodate the NR molecules within the zeolite framework.

Upon further increasing the size of the cation, such as in the case of Cs-Y (d = 1.67 Å),[71] the contribution from the ~550 nm band is clearly reduced (from 22 to 14% from Li-Y to Cs-Y), while the redshifted band completely disappears. This behaviour is rationally explained by the large volume of Cs^+, which competes with NR close to the surface sites of the zeolite. Cs^+ ions have been shown to be too large to pass through the small pore system (sites I and I′).[68] Therefore, Cs^+ should be distributed preferentially at sites II, suggesting that the red-absorbing species may coordinate at these positions, which is inhibited by the presence of Cs^+. Thus, NR packing within the inner cavities of the Cs-Y zeolite is favoured, as suggested by the increased contributions of the H-aggregate, monomer, and J-aggregate bands.

To further characterize the distribution of NR populations within the used zeolites, we studied all the composites at different initial concentrations of the dye. Figure 4S shows the DT spectra of NR interacting with the CBV 500, CBV 300, and Cs-Y zeolites. No significant changes at varying initial concentrations were observed in the absorption profiles, except for CBV 100 (Figure 1C). For CBV 100, as the NR concentration decreases from 2×10^{-5} to 2×10^{-6} M, the monomers and J-aggregates are favoured with respect to the H-aggregates and the weakly interacting species. This observation was also confirmed by the deconvolution analysis of the DT spectra, where the contributions from the monomers and J-aggregates to the total spectrum increased from 17 to 21% and from 22 to 32%, respectively. On the other hand, the H-aggregate contribution is reduced from 31 to 27%, while the contribution of J-aggregates-2 remains nearly constant (~4%). The relative intensity of the weakly interacting NR species also decreases from 22 to 16%. Finally, no redshifted band was detected at the lowest concentration of NR. The observed changes, observed only for the least acidic zeolite (CBV 100), are ascribed to the larger dye occupancy sites, and, therefore, to a partial disaggregation of the dye (in the case of the H-aggregates), favouring interactions with the zeolite walls (monomers and J-aggregates).

2.1.4. Steady-State Emission Spectra of NR Interacting with the CBV and the Metal-Ion-Exchanged M-Y (M = Li^+, Mg^{2+}, Cs^+) Zeolites

Figure 2 shows the steady-state UV-visible emission spectra of NR (2×10^{-5} M) in the presence of (A): (1) CBV 500, (2) CBV 300, and (3) CBV 100 and (B): (1) Li-Y, (2) Mg-Y, and (3) Cs-Y in DCM suspensions upon excitation at 600 nm (region mainly containing H-aggregates and monomers). The emission (λ_{exc} = 470 nm) from the free dye in pure DCM is also shown for comparison. The spectra of the composites show a main band with a maximum intensity at ~670 nm and a shoulder at ~725 nm. These features are redshifted (1520-1840 and 1820 cm^{-1} for the CBV and the M-Y zeolites, respectively) in comparison to the emission of the dye in pure DCM. The redshift is due to the formation of H bonds and aggregates, which also reduce the fluorescence intensity due to the presence of ICT and additional non-radiative decay channels, such as self-quenching processes.[52] We assign the main band (λ_{max} ~670 nm) to the emission of NR monomers interacting with the zeolite framework, while the shoulder at ~725 nm is ascribed to the J-aggregates formed inside the zeolite framework. No clear contribution from the H-aggregates is observed in the fluorescence spectra due to their forbidden excitonic transitions and thus short lifetime, which reduces their steady-state emission intensity.[52] Finally, the excitation at 750 nm of both the DCM-washed and unwashed NR:zeolite complexes were recorded. The washed samples did not display any clear emission at this excitation wavelength, while the unwashed samples showed a new, weak emission band at ~770 nm. As an example, the excitation of unwashed NR/CBV 300 is reported in Figure 2A (black dashed line). This mismatched emission behaviour between the washed and the unwashed samples is explained by a low number of red-absorbing species in the washed sample (*vide supra*), along with a lower fluorescence quantum yield. The emission decays will provide additional information (*vide infra*).

Before studying the emission decays, we explored the concentration effect on the emission spectra of the NR:zeolite composites. As suggested by the DT spectra (Section 2.1.4.), the emission behaviours of NR interacting with CBV 500 and CBV 300 do not depend on the initial concentration of the dye, and the fluorescence spectra preserve similar shapes (Figure 5SA and 5SB). On the other hand, in presence of CBV 100 and using different initial NR concentrations (from 2×10^{-5} to 2×10^{-6} M), we observed a hypsochromic shift of the emission when the dye concentration decreases (Figure 2C). This shift reflects the higher contribution of the monomers to the total emission spectrum. Surprisingly, we found a concentration dependence of the emission spectrum

for NR/Cs-Y (Figure 5SC); however, the DT does not undergo noticeable changes (Section 2.1.4. and Figure 4SC). Upon decreasing the initial dye concentration, the emission blue shifts, indicating a higher contribution of monomers (549 nm) to the total fluorescence. This difference, not observed from the DT spectra, could be due to an increase of the fluorescence quantum yield of the monomers at lower dye concentrations.

2.2. Time-Resolved Emission Measurements

2.2.1. Emission Decays of NR Interacting with the CBV Zeolites (CBV 500, CBV 300, CBV 100) in DCM Suspensions

The photodynamic properties of fluorescent probes are typically influenced by the host environment. To obtain insights into the dynamics of NR interacting with the studied CBV zeolites, we performed picosecond-resolved emission measurements upon excitation at 635 (region corresponding to the monomers and H- and J-aggregates) and 750 (region corresponding to the red-absorbing species) nm. In pure DCM, the emission decay of NR shows a single component with a lifetime of 4.4 ns, corresponding to the emission of the CS state formed by excitation of the dye.[52] Note that at 635 nm we do not excite free NR, as it absorbs at shorter wavelengths. Figure 3A shows the emission decays of the NR/CBV complexes excited at 635 and 750 nm recording at 700 and 810 nm. Table 1 and Table 4S give the values of the emission lifetimes (τ_i) obtained from multi-exponential fits of the experimental results. For all the studied composites, the fits give three decaying components, with values (pre-exponential factors at 700 nm, A_i%) of τ_1 = 90, 76, and 80 ps (36, 38, and 36%), τ_2 = 0.42, 0.38, and 0.39 ns (55, 51, and 43%), and τ_3 = 1.43, 1.19, and 1.07 ns (9, 11, and 21%) for NR interacting with CBV 500, CBV 300, and CBV 100, respectively.

Following excitonic theory, the H-aggregate lifetime should be shorter than the J-aggregate lifetime due to their forbidden transition. Thus, we ascribe the longest lifetime, τ_3, to the monomers, while τ_1 and τ_2 correspond to the lifetimes of the H- and J-aggregates, respectively. Notably, the number of components obtained from the fit of the emission decays well matches the number of NR populations excited at 635 nm (see Figure 2SA, 2SB, and 2SC). Therefore, τ_1, τ_2, and τ_3 represent the average emission lifetimes of the collection of H-aggregates, J-aggregates and monomers, respectively.

The emission lifetimes slightly decrease from CBV 500 to CBV 100. As stated in Section 2.1.2., among the studied CBV zeolites, CBV 100 contains the most Na^+ cations in the framework. As a result, the high number of charge-compensating cations in CBV 100 gives the smallest available volume for the guest, thus favouring increments of self-quenching and other non-radiative relaxation processes as well as stronger guest-host interactions. From the amplitudes of each component at all the observed wavelengths, in all three systems, the monomers have the smallest contribution to the species located in the zeolite framework (Table 4S). The amplitudes of the emission decay components for the H- and J-aggregates do not show a systematic dependence on the observation wavelength, while those of monomers decrease in the red section of the emission spectrum (for CBV 500 and CBV 300) or remain constant (for CBV 100).

2.2.2. Emission Decays of NR Interacting with the Metal-Ion-Exchanged M-Y (M = Li^+, Mg^{2+}, Cs^+) Zeolites

In the presence of the metal-ion-exchanged M-Y zeolites with excitation at 635 nm (region corresponding to the monomers and H- and J-aggregates), we observed multi-exponential behaviours in the emission decays of the composites (Figure 3B). The obtained lifetime values are τ_1 = 183, 130, and 224 ps; τ_2 = 0.67, 0.57, and 0.73 ns; τ_3 = 1.50, 1.42, and 1.48 ns for NR interacting with Li-Y, Mg-Y, and Cs-Y, respectively (Table 1 and Table 4S).

Similar to the CBV zeolites, we assign the longest lifetime (τ_3) to the emission of the monomers interacting with the framework, while τ_1 and τ_2 correspond to the H- and J-aggregates, respectively. The lifetimes of the monomers are similar to those found for the precursor CBV 500. Thus, metal-ion exchange does not significantly affect the emission behaviour of this species. In contrast, the H- and J-aggregates display slower dynamics in presence of the metal cations. The longer time constants for NR/Li-Y are likely due to the higher polarizing power of Li^+, whose strong electric field might provoke a distortion in the position/orientation of the aggregates, thus affecting (in this case, weakening) their intermolecular interactions. The presence of such polarizing cations near the excited NR molecules should theoretically affect their electronic transitions, as the NR transition involves a charge-transfer process followed by fast electronic redistribution. On the other hand, in presence of Cs-Y, the large size of Cs^+ could induce a partial or even total breakage of the aggregates, thus reducing/disrupting

their interactions and increasing their emission lifetimes in their detection region. In this case, monomers are the favoured species, showing the highest contribution (Table 4S). Finally, for NR/Mg-Y, we would expect the strongest interaction of Mg^{2+} with the aggregates due to the small size of the ion and its double charge. In contrast, we observed shorter lifetimes for both the H- and J-aggregates, which is explained by the different locations of Mg^{2+} and Li^{+} within the zeolite framework. Particularly, small divalent cations, such as Ni^{2+}, Mg^{2+}, and Cu^{2+}, tend to locate in site I to be stabilized by the six oxygen atoms, while monovalent cations, such as Li^{+} and Cu^{+}, can be reasonably stabilized by only three oxygen atoms in site I′.[69] The different positions of Li^{+} and Mg^{2+} might explain the differences observed in the lifetime values; the Li^{+} ions are likely closer to the NR aggregates and exert a greater effect on them. However, a direct comparison between the three M-Y zeolites is not easy because the concentrations of the exchange cations are not comparable (see the syntheses of the M-Y zeolites in the SI).

2.2.3. Concentration Effect on the Emission Decays of NR Interacting with CBV 100 Zeolite

Picosecond-resolved emission experiments were performed to study the photobehaviours of the guest populations at different initial concentrations (from 2×10^{-6} to 2×10^{-5} M). Figures 3C, 6SA, and 6SB, together with Table 2, show the results. The lack of concentration dependences of the steady-state behaviours of the NR/CBV 500 and NR/CBV 300 hybrids is also reflected in the time-resolved decay analysis, where the obtained lifetimes for the employed concentrations are very similar.

On the other hand, for the NR/CBV 100 composite, a clear change in the emission decays with varying initial NR concentrations was observed. When the dye concentration decreases from 2×10^{-5} to 9×10^{-6} M, the lifetimes approximately double their value: τ_1 = 80 and 171 ps, τ_2 = 0.39 and 0.72 ns, and τ_3 = 1.07 and 2.08 ns for $[NR]_0 = 2 \times 10^{-5}$ and 9×10^{-6} M, respectively. Upon further decreasing the concentration to 2×10^{-6} M, the emission decays become bi-exponential with time constants of τ_1 = 0.53 ns and τ_2 = 2.22 ns, corresponding to the emission from the J-aggregates and monomers, respectively, while no fluorescence from the H-aggregates is detected. At lower concentrations, the interaction between the dye molecules becomes weaker, and hence, emission quenching is less probable.

Finally, the decay analysis for the NR/Cs-Y composite reveals a lack of H-aggregate contribution to the total emission signal when the initial concentration of NR decreases (Figure 6SC and Table 2). The J-aggregates and monomers are characterized by time constants (τ_1 and τ_2) of 0.50 and 1.67 ns, respectively.

2.3. Femtosecond Time-Resolved Emission Measurements

2.3.1. Femtosecond Dynamics of NR Interacting with the CBV Zeolites (CBV 500, CBV 300, CBV 100) and Metal-Ion-Exchanged M-Y Zeolites (M = Li^+, Mg^{2+}, Cs^+) in DCM Suspensions

We used femtosecond-fluorescence up-conversion spectroscopy to unravel the ultrafast photodynamics of NR within the studied zeolites. Figure 4 shows the transient emission decays of the NR:zeolite complexes upon excitation at 562 nm (region corresponding to the weakly interacting NR) with observation at 630 nm and 700 nm (for additional wavelengths of observation, see Figure 7S). Table 3 gives the results of the multi-exponential fits of the transient decays for all the composites. The NR dynamics within the studied zeolites show bi-exponential behaviour at the bluest region of the emission spectrum (630-650 nm) and a constant offset (τ_3 in Table 3), which was fixed during the fit to the shortest time found in the picosecond emission studies. The time constants do not significantly change with the various hosts, with time constants of τ_1 = 166-206 fs and τ_2 = 1.30-1.56 ps and τ_1 = 145-170 fs and τ_2 = 1.09-2.32 ps for NR interacting with the CBV and the M-Y zeolites, respectively.

At longer observation wavelengths (670-700 nm), τ_1 is characterized by a rising component (Figure 8S), indicating a common channel for both the blue and red dynamics, which are assigned to the ICT of NR.[52] The ultrafast photobehaviour of NR in pure DCM is characterized by a single rising component with a lifetime of ~1 ps and a long offset resolved by the picosecond experiments (4.4 ns) in the 630-730 nm range.[52] The rising component in the suspensions is assigned to the formation of a CS state due to the ICT process occurring in the excited NR molecules. This assignment is in agreement with another report showing that the locally excited (LE) state of NR, which is formed within the excitation pulse, can relax by emission and/or ICT from the diethylamino to the carbonyl group, thus generating a CS structure.[52] The shortening of the ICT process for NR in presence of a zeolite host compared to the free dye in DCM (~1 ps) is explained by the increase of both the polarity and the H-bonding ability

of the medium, which, in turn, decrease the energy barrier between the LE and CS states. As a result, the CS state forms with higher efficiencies.[52] The second component (τ_2) is attributed to a vibrational cooling (VC) process at the S_1 level of the CS state. Scheme 2 summarizes the observed dynamics for metal-ion-exchanged zeolites containing NR monomers, H- and J-aggregates. Importantly, the obtained values represent averages of the relaxation times for the excited-state NR species. Due to the presence of multiple populations with different orientations and interactions in the framework, the results are likely a combination of all the contributions from the existing populations.

2.3.2. Concentration Effect on the Femtosecond-Emission Dynamics of NR Interacting with the CBV 100 Zeolite

Figure 4C shows the transient femtosecond-emission decays of NR at different initial concentrations (2×10^{-5}-2×10^{-6} M) interacting with CBV 100. In the 630-650 nm region, no variation of either the fast or ultrafast dynamics with the concentration was observed. However, in the middle of the emission spectrum, a very short decay of < 100 fs appears between 670 and 689 nm, together with an offset. This contribution is higher for the lowest concentration, completely disappearing at 700 nm. The observed ultrafast component is clearly present at low concentrations of NR, while the component is not visible at the highest loading. Thus, this component arises due to a strong specific and localized interaction between the NR monomers with the CBV 100 framework. The lack of this component at the highest initial NR concentration and at other wavelengths of observation is explained by the stronger emissions of the other NR populations (for example, J-aggregates) that overlap with the contribution of the interacting monomers. Recently, the ultrafast dynamics of (E)-2-(2-hydroxybenzyliden)amino-4-nitrophenol (HBA-4NP) aggregates interacting with the NaY zeolite were observed to be affected by the initial concentration of the sample.[30] Particularly, for concentrated solutions, the guest-guest interactions slowed the photobehaviour of the interrogated species with respect to the diluted samples.

2.4. Discussion of the Behaviour of NR within the Zeolite and Mesoporous Materials

Now, we will discuss the behaviour of NR in the studied CBV zeolites and compare this behaviour with those previously reported using R-MCM41 and Al-MCM41 mesoporous materials.[52] Table 4 shows the time constants of the related fast and ultrafast dynamics of excited NR in presence of the mesoporous and zeolite materials. Table 4 also gives the values of some parameters of the host (pore/cavity diameter, SiO_2/Al_2O_3 molar ratio, and Brunauer-Emmett-Teller (BET) surface area) and the loading efficiency for each formed complex. To make a fair comparison of the obtained results, we must recall the main differences between the investigated hosts, i.e., the structure (hexagonal for R-MCM41 and Al-MCM41 and tetragonal for the CBV zeolites) and the composition (silanol groups for R-MCM41 and Al-MCM41 and Na^+ cations and Al atoms for the CBV zeolites).

First, the molecular packing is more efficient in the zeolite nanocages despite their reduced dimensions (pore/cavity diameters of 35 and ~13 Å for the mesoporous materials and the zeolites, respectively) and BET areas (1000 and 970 m^2/g for R-MCM41 and Al-MCM41, respectively; 750, 925, and 900 m^2/g for CBV 500, CBV 300, and CBV 100, respectively) with respect to the MCM41-based materials (Table 4). In fact, the loading efficiencies obtained for the zeolites (2.4, 2.5, and 2.6 × 10^{18} NR molecules/$g_{zeolite}$ for CBV 500, CBV 300, and CBV 100, respectively) are higher than those calculated for the mesoporous materials (1.9 and 2.0 × 10^{18} NR molecules/g_{MCM41} for R-MCM41 and Al-MCM41, respectively) under the same experimental conditions (Table 4). These differences are due to electrostatic interactions between the encapsulated NR and the Na^+ cations and the aluminosilicate framework of the zeolite cavity, which facilitate molecular trapping.[30]

Both the spectral absorption and emission properties of NR interacting with the zeolite and MCM41 mesoporous materials are comparable in terms of the redshifts and broadening of the DT spectra (Table 3S and Ref. 52). Therefore, we expect that the dye exhibits similar interactions within the two types of hosts. However, while the distributions of the caged NR monomers and H-aggregates show very similar values, the distribution of J-aggregates is higher within the MCM41 mesoporous materials (Table 3S and Ref. 52) due to the higher surface acidity of these hosts, whose SiOH groups enhance H-bonding with the NR molecules.[52]

The increased rates of both the fast and ultrafast dynamics for the excited NR/CBV complexes compared to the rates for the NR/X-MCM41 complexes reflect the stronger host-guest interactions in the zeolite framework (Table 4). The emission lifetimes of the H-aggregates (τ_1 in Table 4) are shortened by more than three times their initial value between the mesoporous and zeolite materials (τ_1 = 320 and 310 ps for NR with R-MCM41 and Al-MCM41, respectively; τ_1 = 90, 76, and 80 ps for NR with CBV 500, CBV300, and CBV 100, respectively, Table 4). Less drastic but evident changes are also present for the J-aggregates and monomers, whose emission lifetimes in the mesoporous materials (~1 and ~2.5 ns, respectively) decrease to ~0.4 and ~1.2 ns in the zeolite framework (Table 4). Upon interaction of NR with the MCM41 mesoporous materials, the ICT process occurs within ~300 fs, while within the zeolite, this process is reduced to ~200 fs (Table 4). The VC process is also accelerated from the mesoporous (~3 ps) to zeolite (~1.5 ps) materials. The emission from the ICT state is strongly influenced by the energy gap of the excited state and CS state. Since the gap between the LE and CS states depends on the donor and acceptor strengths, the interaction of these groups with the environment is crucial. Recently, the computed S_1 potential-energy surfaces of a complex of NR with two water molecules showed that H bonds stabilize the CS state and lower the energy barrier for the LE to CS state transition.[37] Within the zeolite cavities, the spatial restriction strengthens the host-guest and guest-guest specific and non-specific interactions, and as a result, the ICT process occurs more efficiently. The restricted motion also increases the vibronic coupling between the S_1 and S_0 states, thus enhancing the non-radiative deactivation pathways.[72] This effect is confirmed by the shortened time constants of the VC process in the NR/CBV composites.

3. Conclusions

In this study, we investigated the photophysics of NR interacting with NaY-type zeolites containing different Na/Al ratios and charge-balancing metal cations in DCM suspensions using steady-state absorption and emission and time-resolved spectroscopy techniques. The results showed that the interaction of the dye with these materials leads to the formation of different ground-state populations of NR (monomers, H- and J-aggregates, and surface-adsorbed species) whose contributions to the total spectrum

depend on the Na^+ content and the metal doping ratio. Large bathochromic shifts characterized both the absorption and emission spectra of the NR:zeolite complexes. Time-resolved picosecond emission measurements revealed multi-exponential behaviours for the studied compounds, while in pure DCM, the emission decays were fitted using a single-exponential function. The changes observed in the steady-state and the photodynamic properties of the investigated samples were explained in terms of the Brønsted (H-bond formation) and Lewis host-guest interactions and dimensions/polarizing properties of the exchanged cation. The femtosecond results indicated that the initially formed LE state of NR gives rise to a CS state within ~200 fs, followed by a VC process of ~1-2 ps. A comparison of the present results with previous ones obtained using MCM41-based materials show that the host-guest and guest-guest specific and non-specific interactions as well as the spatial restriction to motion of the guest play important roles in controlling the photobehaviours of the formed composites.

The above findings indicate the potential use of NR to probe the various acidic sites of the studied NaY-type zeolites, which may contribute to the design of zeolite-based metal-ion sensors and a better understanding of the field of nanocatalysis.

Acknowledgments

This work was supported by the JCCM and MINECO through projects: PEII-2014-003-P, Consolider Ingenio 2010 (CSD2009-0050, MULTICAT), and MAT2014-57646-P. A. Corma and M.T. Navarro thank the MINECO (Severo Ochoa program SEV-2012-0267 and MAT2015-71842-P) for financial support.

Supplementary Materials

Table 1S displays the characteristics of the studied zeolites. Table 2S shows the Nile Red (NR) loading efficiencies for the studied zeolites. Figure 1S exhibits an example of the UV-visible absorption spectra of a sample before and after washed. Table 3S shows the UV-visible absorption maxima of the different NR population within the studied zeolites in DCM suspensions. Figure 2S displays the deconvolution of the UV-visible DT spectra of NR interacting with A) CBV 500, B) CBV 300, C) CBV 100, D) Li-Y, E) Mg-Y, and F) Cs-Y in DCM suspensions. Figure 3S shows the UV-visible DT deconvolution spectra of NR/CBV 100 at different initial NR concentrations: (A) 9×10^{-6} M and (B) 2×10^{-6} M. Figure 4S and 5S exhibit the absorption and emission

spectra respectively of (A) CBV 500, (B) CBV 300, and (C) Cs-Y in DCM suspensions at different initial NR concentrations. Table 4S displays the fluorescence emission lifetimes of NR interacting with the different zeolites in DCM suspensions. Table 5S shows the fluorescence emission lifetimes of NR interacting with CBV 300 upon excitation at 750 nm. Figure 6S shows the magic-angle emission decays of NR interacting with (A) CBV 500, (B) CBV 300, and (C) Cs-Y in DCM suspensions at different initial NR concentrations. Figure 7S exhibits emission transient decays of NR interacting with (A) CBV 500, (B) CBV 300, (C) CBV 100, (D) Li-Y, (E) Mg-Y, and (F) Cs-Y in DCM suspensions. Figure 8S shows a comparison of the emission transient decays between 630 nm and 700 nm of observation wavelength of NR interacting with (A) CBV 500, (B) CBV 300, (C) CBV 100, (D) Li-Y, (E) Mg-Y, and (F) Cs-Y in DCM suspensions.

References

[1] W. Hölderich, M. Hesse, F. Näumann, Zeolites: Catalysts for Organic Syntheses, Angew. Chem. Int. Ed., 27 (1988) 226-246.
[2] K.B. Yoon, Electron- and charge-transfer reactions within zeolites, Chem. Rev., 93 (1993) 321-339.
[3] D. Barthomeuf*, Basic Zeolites: Characterization and Uses in Adsorption and Catalysis., Catal. Rev. Sci. Eng., 38 (1996) 521-612.
[4] V. Ramamurthy, P. Lakshminarasimhan, C.P. Grey, L.J. Johnston, Energy transfer, proton transfer and electron transfer reactions within zeolites, Chem. Commun., (1998) 2411-2424.
[5] M. Pauchard, A. Devaux, G. Calzaferri, Dye-loaded zeolite L sandwiches as artificial antenna systems for light transport, Chem. Eur. J., 6 (2000) 3456−3470.
[6] Y. Xia, B. Gates, Y. Yin, Y. Lu, Monodispersed colloidal spheres: Old materials with new applications, Adv. Mater., 12 (2000) 693-713.
[7] G. Calzaferri, M. Pauchard, H. Maas, S. Huber, A. Khatyr, T. Schaafsma, Photonic antenna system for light harvesting, transport and trapping, J. Mater. Chem., 12 (2002) 1-13.
[8] B. Muñoz, A. Rámila, J. Pérez-Pariente, I. Díaz, M. Vallet-Regí, MCM-41 organic modification as drug delivery rate regulator, Chem. Mater., 15 (2003) 500-503.

[9] H.S. Kim, S.M. Lee, K. Ha, C. Jung, Y.J. Lee, Y.S. Chun, D. Kim, B.K. Rhee, K.B. Yoon, Aligned Inclusion of Hemicyanine Dyes into Silica Zeolite Films for Second Harmonic Generation, J. Am. Chem. Soc., 126 (2004) 673-682.
[10] D. Brühwiler, G. Calzaferri, Molecular sieves as host materials for supramolecular organization, Microporous Mesoporous Mater., 72 (2004) 1-23.
[11] Y. Kim, A. Das, H. Zhang, P.K. Dutta, Zeolite membrane-based artificial photosynthetic assembly for long-lived charge separation, J. Phys. Chem. B, 109 (2005) 6929-6932.
[12] M. Vallet-Regí, Ordered mesoporous materials in the context of drug delivery systems and bone tissue engineering, Chem. Eur. J., 12 (2006) 5934-5943.
[13] M. Vallet-Regí, F. Balas, D. Arcos, Mesoporous materials for drug delivery, Angew. Chem. Int. Ed., 46 (2007) 7548-7558.
[14] M.-H. Sun, S.-Z. Huang, L.-H. Chen, Y. Li, X.-Y. Yang, Z.-Y. Yuan, B.-L. Su, Applications of hierarchically structured porous materials from energy storage and conversion, catalysis, photocatalysis, adsorption, separation, and sensing to biomedicine, Chem. Soc. Rev., 45 (2016) 3479-3563.
[15] S. Mintova, M. Jaber, V. Valtchev, Nanosized microporous crystals: emerging applications, Chem. Soc. Rev., 44 (2015) 7207-7233.
[16] F. Marlow, J. Caro, On the anisotropy of the optical properties of zeolites loaded with organic molecules, Zeolites, 12 (1992) 433-434.
[17] J.C. Scaiano, H. García, Intrazeolite photochemistry: Toward supramolecular control of molecular photochemistry, Acc. Chem. Res., 32 (1999) 783-793.
[18] N.J. Turro, From boiling stones to smart crystals: Supramolecular and magnetic isotope control of radical-radical reactions in zeolites, Acc. Chem. Res., 33 (2000) 637-646.
[19] M. Pauchard, S. Huber, R. Meańdallet-Renault, H. Maas, R. Pansu, G. Calzaferri, Time- and space-resolved luminescence of a photonic dye - Zeolite antenna, Angew. Chem. Int. Ed., 40 (2001) 2839-2842.
[20] H. García, H.D. Roth, Generation and reactions of organic radical cations in zeolites, Chem. Rev., 102 (2002) 3947-4007.
[21] J.K. Thomas, Physical aspects of photochemistry and radiation chemistry of molecules adsorbed on silica, .gamma.-alumina, zeolites, and clays, Chem. Rev., 93 (1993) 301-320.
[22] R.A. Schoonheydt, P. Geerlings, E.A. Pidko, R.A. Van Santen, The framework basicity of zeolites, J. Mater. Chem., 22 (2012) 18705-18717.
[23] S. Hashimoto, Zeolite photochemistry: Impact of zeolites on photochemistry and feedback from photochemistry to zeolite science, J. Photochem. Photobiol., C, 4 (2003) 19-49.
[24] V. Ramamurthy, Controlling photochemical reactions via confinement: Zeolites, J. Photochem. Photobiol., C, 1 (2000) 145-166.
[25] M. Gil, M. Ziółek, J.A. Organero, A. Douhal, Confined Fast and Ultrafast Dynamics of a Photochromic Proton-Transfer Dye within a Zeolite Nanocage, J. Phys. Chem. C, 114 (2010) 9554-9562.
[26] M. Gil, J.A. Organero, E. Peris, H. García, A. Douhal, Confinement effect of nanocages and nanotubes of mesoporous materials on the keto forms photodynamics of Sudan I, Chem. Phys. Lett., 474 (2009) 325-330.
[27] M. Gil, S. Wang, J.A. Organero, L. Teruel, H. Garcia, A. Douhal, Femtosecond dynamics within nanotubes and nanocavities of mesoporous and zeolite materials, J. Phys. Chem. C, 113 (2009) 11614-11622.

[28] N. Alarcos, B. Cohen, A. Douhal, Photodynamics of a proton-transfer dye in solutions and confined within NaX and NaY zeolites, J. Phys. Chem. C, 118 (2014) 19431-19443.
[29] N. Alarcos, J.A. Organero, F. Sánchez, A. Douhal, Exploring the Photobehavior of Nanocaged Monomers and H- and J-Aggregates of a Proton-Transfer Dye within NaX and NaY Zeolites, J. Phys. Chem. C, 118 (2014) 8217-8226.
[30] N. Alarcos, F. Sánchez, A. Douhal, Interrogating ultrafast dynamics of a salicylideneaniline derivative within faujasite zeolites, Chem. Phys. Lett., (2017).
[31] H.B. Hetzer, Titrimetric and equilibrium studies using indicators related to nile blue A, Anal. Chem., 38 (1966) 451-461.
[32] V.G. Machado, R.I. Stock, C. Reichardt, Pyridinium N-phenolate betaine dyes, Chem. Rev., 114 (2014) 10429-10475.
[33] J. Jose, K. Burgess, Benzophenoxazine-based fluorescent dyes for labeling biomolecules, Tetrahedron, 62 (2006) 11021-11037.
[34] A.K. Dutta, K. Kamada, K. Ohta, Spectroscopic studies of nile red in organic solvents and polymers, J. Photochem. Photobiol., A, 93 (1996) 57-64.
[35] A. Cser, K. Nagy, L. Biczók, Fluorescence lifetime of Nile Red as a probe for the hydrogen bonding strength with its microenvironment, Chem. Phys. Lett., 360 (2002) 473-478.
[36] A. Kawski, B. Kukliński, P. Bojarski, Photophysical properties and thermochromic shifts of electronic spectra of Nile Red in selected solvents. Excited states dipole moments, Chem. Phys., 359 (2009) 58-64.
[37] A.Y. Freidzon, A.A. Safonov, A.A. Bagaturyants, M.V. Alfimov, Solvatofluorochromism and twisted intramolecular charge-transfer state of the nile red dye, Int. J. Quantum Chem., 112 (2012) 3059-3067.
[38] A.J. Carmichael, K.R. Seddon, Polarity study of some 1-alkyl-3-methylimidazolium ambient-temperature ionic liquids with the solvatochromic dye, Nile Red, J. Phys. Org. Chem., 13 (2000) 591-595.
[39] C. Martin, S. Bhattacharyya, A. Patra, A. Douhal, Single and multistep energy transfer processes within doped polymer nanoparticles, Photochem. Photobiol. Sci., 13 (2014) 1241-1252.
[40] C. Martiń, M.R. Di Nunzio, B. Cohen, A. Douhal, Location and freedom of single and double guest in dye-doped polymer nanoparticles, Photochem. Photobiol. Sci., 13 (2014) 1580-1589.
[41] E. Fleige, B. Ziem, M. Grabolle, R. Haag, U. Resch-Genger, Aggregation phenomena of host and guest upon the loading of dendritic core-multishell nanoparticles with solvatochromic dyes, Macromolecules, 45 (2012) 9452-9459.
[42] P. Hazra, D. Chakrabarty, A. Chakraborty, N. Sarkar, Intramolecular charge transfer and solvation dynamics of Nile Red in the nanocavity of cyclodextrins, Chem. Phys. Lett., 388 (2004) 150-157.
[43] N.C. Maiti, M.M.G. Krishna, P.J. Britto, N. Periasamy, Fluorescence dynamics of dye probes in micelles, J. Phys. Chem. B, 101 (1997) 11051-11060.
[44] A. Datta, D. Mandal, S.K. Pal, K. Bhattacharyya, Intramolecular charge transfer processes in confined systems. Nile red in reverse micelles, J. Phys. Chem. B, 101 (1997) 10221-10225.
[45] P. Greenspan, E.P. Mayer, S.D. Fowler, Nile red: A selective fluorescent stain for intracellular lipid droplets, J. Cell Biol., 100 (1985) 965-973.
[46] D.L. Sackett, J. Wolff, Nile red as a polarity-sensitive fluorescent probe of hydrophobic protein surfaces, Analytical Biochemistry, 167 (1987) 228-234.

[47] M.L. Ferrer, F. Del Monte, Enhanced emission of nile red fluorescent nanoparticles embedded in hybrid sol-gel glasses, J. Phys. Chem. B, 109 (2005) 80-86.
[48] A.M. Bardo, M.M. Collinson, D.A. Higgins, Nanoscale properties and matrix-dopant interactions in dye-doped organically modified silicate thin films, Chem. Mater., 13 (2001) 2713-2721.
[49] H. Tajalli, A.G. Gilani, M.S. Zakerhamidi, P. Tajalli, The photophysical properties of Nile red and Nile blue in ordered anisotropic media, Dyes Pigm., 78 (2008) 15-24.
[50] R. Mellaerts, M.B.J. Roeffaers, K. Houthoofd, M. Van Speybroeck, G. De Cremer, J.A.G. Jammaer, G. Van Den Mooter, P. Augustijns, J. Hofkens, J.A. Martens, Molecular organization of hydrophobic molecules and co-adsorbed water in SBA-15 ordered mesoporous silica material, Phys. Chem. Chem. Phys., 13 (2011) 2706-2713.
[51] T. Felbeck, T. Behnke, K. Hoffmann, M. Grabolle, M.M. Lezhnina, U.H. Kynast, U. Resch-Genger, Nile-Red–Nanoclay Hybrids: Red Emissive Optical Probes for Use in Aqueous Dispersion, Langmuir, 29 (2013) 11489-11497.
[52] C. Martín, P. Piatkowski, B. Cohen, M. Gil, M.T. Navarro, A. Corma, A. Douhal, Ultrafast Dynamics of Nile Red Interacting with Metal Doped Mesoporous Materials, J. Phys. Chem. C, 119 (2015) 13283-13296.
[53] C. Martin, B. Cohen, M.T. Navarro, A. Corma, A. Douhal, Unraveling the ultrafast behavior of nile red interacting with aluminum and titanium co-doped MCM41 materials, Phys. Chem. Chem. Phys., 18 (2016) 2152-2163.
[54] N. Sarkar, K. Das, D.N. Nath, K. Bhattacharyya, Twisted charge transfer process of Nile Red in homogeneous solution and in faujasite zeolite, Langmuir, 10 (1994) 326-329.
[55] J.A. Organero, L. Tormo, A. Douhal, Caging ultrafast proton transfer and twisting motion of 1-hydroxy-2-acetonaphthone, Chem. Phys. Lett., 363 (2002) 409-414.
[56] F. Ye, M.M. Collinson, D.A. Higgins, What can be learned from single molecule spectroscopy? Applications to sol-gel-derived silica materials, Phys. Chem. Chem. Phys., 11 (2009) 66-82.
[57] M. Busby, C. Blum, M. Tibben, S. Fibikar, G. Calzaferri, V. Subramaniam, L. De Cola, Time, space, and spectrally resolved studies on J-aggregate interactions in zeolite L nanochannels, J. Am. Chem. Soc., 130 (2008) 10970-10976.
[58] F. Nüesch, J.E. Moser, V. Shklover, M. Grätzel, Merocyanine aggregation in mesoporous networks, J. Am. Chem. Soc., 118 (1996) 5420-5431.
[59] K.A.W.Y. Cheng, N.P. Schepp, F.L. Cozens, Ultrafast dynamics of pyrene excimer formation in Y zeolites, J. Phys. Chem. A, 108 (2004) 7132-7134.
[60] K.A.W.Y. Cheng, N.P. Schepp, F.L. Cozens, Resolution of ultrafast pyrene excimer emission rise times in zeolites X and Y, Photochem. Photobiol., 82 (2006) 132-138.
[61] A. Mishra, R.K. Behera, P.K. Behera, B.K. Mishra, G.B. Behera, Cyanines during the 1990s: a review, Chem. Rev., 100 (2000) 1973-2011.
[62] M. Kasha, H.R. Rawls, M.A. El-Bayoumi, The Exciton Model In Molecular Spectroscopy, Pure Appl. Chem., 11 (1965) 371-392.
[63] N. Alarcos, F. Sánchez, A. Douhal, Spectroscopy and relaxation dynamics of salicylideneaniline derivative aggregates encapsulated in MCM41 and SBA15 pores, Microporous Mesoporous Mater., 226 (2016) 34-43.
[64] N. Alarcos, F. Sánchez, A. Douhal, Confinement effect on ultrafast events of a salicylideneaniline derivative within mesoporous materials, Microporous Mesoporous Mater., 248 (2017) 54-61.
[65] T.K. Phung, G. Busca, On the Lewis acidity of protonic zeolites, Appl. Catal., A, 504 (2015) 151-157.

[66] D.L. Bhering, A. Ramírez-Solís, C.J.A. Mota, A density functional theory based approach to extraframework aluminum species in zeolites, J. Phys. Chem. B, 107 (2003) 4342-4347.
[67] L. Intriago, E. Díaz, S. Ordóñez, A. Vega, Combustion of trichloroethylene and dichloromethane over protonic zeolites: Influence of adsorption properties on the catalytic performance, Microporous Mesoporous Mater., 91 (2006) 161-169.
[68] P. Chu, The deammoniation reaction of ammonium Y zeolite, J. Catal., 43 (1976) 346-352.
[69] T. Frising, P. Leflaive, Extraframework cation distributions in X and Y faujasite zeolites: A review, Microporous Mesoporous Mater., 114 (2008) 27-63.
[70] C. Laborde-Boutet, G. Joly, A. Nicolaos, M. Thomas, P. Magnoux, Selectivity of Thiophene/Toluene Competitive Adsorptions onto Zeolites. Influence of the Alkali Metal Cation in FAU(Y), Ind. Eng. Chem. Res., 45 (2006) 8111-8116.
[71] R.D. Shannon, Revised effective ionic radii and systematic studies of interatomic distances in halides and chalcogenides, Acta Crystallogr., Sect. A: Found. Crystallogr., 32 (1976) 751-767.
[72] F. Márquez, H. García, E. Palomares, L. Fernández, A. Corma, Spectroscopic evidence in support of the molecular orbital confinement concept: Case of anthracene incorporated in zeolites, J. Am. Chem. Soc., 122 (2000) 6520-6521.

Tables, Figures, and Schemes

Captions

Table 1. Values of the fluorescence emission lifetimes (τ_i) obtained from a global multi-exponential fit of the emission decays of NR (2×10^{-5} M) interacting with CBV 500, CBV 300, CBV 100, Li-Y, Mg-Y, and Cs-Y in DCM suspensions upon excitation at 635 nm.

Table 2. Values of the fluorescence emission lifetimes (τ_i) and normalized (to 100) pre-exponential factors (A_i) obtained from a global multi-exponential fit of the emission decays of NR at different concentrations interacting with CBV 500, CBV 300, CBV 100, Li-Y, Mg-Y, and Cs-Y in DCM suspensions upon excitation at 635 nm and observing at 700 nm.

Table 3. Values of the time constants (τ_i) and normalized (to 100) pre-exponential factors (A_i) obtained from a global multi-exponential fit of the fs-emission signals of

NR (2×10^{-5} M) interacting with the CBV (CBV 500, CBV 300, CBV 100) and the M-Y (M = Li^+, Mg^{2+}, Cs^+) zeolites in DCM suspensions upon excitation at 562 nm and observing from 630 nm to 700 nm.[a]

Table 4. Values of some parameters, such as pore/cavity diameter, SiO2/Al2O3 mole ratio, BET surface area of the used zeolites (CBV 500, CBV300, and CBV 100) and the mesoporous materials (R-MCM41 and Al-MCM41) from Ref. 52, together with the times of the related fast end ultrafast dynamics upon excitation of their complexes with NR in DCM suspensions. The loading efficiencies are also reported for each formed composite

Figure 1. Normalized (to the maximum of intensity) UV-visible DT spectra of NR (2×10^{-5} M) interacting with (A): (1) CBV 500, (2) CBV 300, (3) CBV 100 and (B): (1) Li-Y, (2) Mg-Y, (3) Cs-Y in DCM suspensions. A comparison with the normalized absorption spectrum of NR in a DCM solution is also shown (black solid line). The inset of (A) shows a picture of CBV zeolite with and without NR.

Figure 2. Normalized (to the maximum of intensity) emission spectra of NR (2×10^{-5} M) interacting with (A): CBV 500, CBV 300, CBV 100 and (B): Li-Y, Mg-Y, Cs-Y in DCM suspensions. The samples were excited at (A, B) 600 and ((A): black dashed line) 750 nm. The comparison with the normalized emission spectrum of NR in a DCM solution (λ_{exc} = 470 nm) is also shown (black solid line). (C) Normalized to the maximum intensity emission spectra of NR/CBV 100 composites at different initial concentrations of NR: (1) 2×10^{-5} M, (2) 9×10^{-6} M, and (3) 2×10^{-6} M.

Figure 3. Normalized (to the maximum of intensity) magic-angles emission decays of NR (2×10^{-5} M) interacting with (A): (1) CBV 500, (2) CBV 300, (3) CBV 100 and (B): (1) Li-Y, (2) Mg-Y, (3) Cs-Y in DCM suspensions upon excitation at (A, B) 635 and ((A): (4)) 750 nm. (C) Normalized to the maximum of intensity magic-angles emission decays of NR interacting with CBV 100 at different initial concentrations: (1) 2×10^{-5} M, (2) 9×10^{-6} M, and (3) 2×10^{-6} M in DCM suspensions upon excitation at 635 nm. The solid lines are from the best multi-exponential fits to the experimental data. IRF is the instrumental response function (~70 ps).The observation wavelengths are ((A): (1), (2), (3), B, C) 700 and ((A): (4)) 810 nm.

Figure 4. Magic-angle femtosecond-emission transient decays of NR (2×10^{-5} M) interacting with different zeolites in DCM suspensions upon excitation at 562 nm and observing at (A) 630 and (B) 700 nm. The solid lines are from the best multi-

exponential fits of the experimental data, and IRF is the instrumental response function (~200 fs). (C) Magic-angle femtosecond-emission transient decays of NR interacting with CBV 100 at different initial concentrations ((■) 2×10^{-5} M, (○) 8×10^{-6} M, and (●) 2×10^{-6} M) in DCM suspensions upon excitation at 562 nm and observing at the wavelengths indicated in the Figure. The solid lines are from the best multi-exponential fits of the experimental data.

Scheme 1. Cartoon showing the different NR populations generated when the dye interacts with the used zeolites.

Scheme 2. Scheme of the energy levels and the lifetimes involved in the intramolecular charge transfer process of NR. LE and CS are the local excited- and charge separated state, respectively.

Table 1

Host	λ_{em}/nm	τ_1/ps	τ_2/ns	τ_3/ns
CBV 500	650-750	90	0.42	1.43
CBV 300	650-750	76	0.38	1.19
CBV 100	650-750	80	0.39	1.07
Li-Y	650-750	183	0.67	1.50
Mg-Y	650-750	130	0.57	1.42
Cs-Y	650-750	224	0.73	1.48

Host	$[NR]_0/10^{-5}$ M	τ_1/ps	A_1/%	τ_2/ns	A_2/%	τ_3/ns	A_3/%

CBV 500	2	90	36	0.42	55	1.43	9
	0.9	90	51	0.48	37	1.61	12
CBV 300	2	76	38	0.38	51	1.19	11
	0.9	72	25	0.38	49	1.39	26
CBV 100	2	80	36	0.39	43	1.07	21
	0.9	171	35	0.72	49	2.08	16
	0.2	---	---	0.53	34	2.22	66
Cs-Y[a]	2	224	30	0.73	34	1.48	36
	0.8	---	---	0.50	37	1.67	63

Table 2

[a]Observation wavelength = 650 nm.

Table 3

Host	λ_{em}/ nm	τ_1/fs (± 50 fs)	A_1/%	τ_2/ps (± 0.5 ps)	A_2/%	τ_3^*/ps	A_3/%
CBV 500	630	190	23	1.3	8	90	69
	640		20		4		76
	650		8		1		91
	670		(-)4		3		93
	700		(-)2		2		96
CBV 300	630	170	21	1.5	11	76	68
	640		16		7		77
	650		10		1		89
	670		(-)6		5		89
	700		(-)1		7		92
CBV 100	630	210	30	1.6	3	80	67
	640		23		3		74
	650		14		4		82
	670		(-)16		6		78
	700		(-)7		1		92
Li-Y	630	170	28	2.3	9	183	63
	640		12		4		84
	650		5		1		94
	670		(-)26		6		68
	700		(-)8		1		91
Mg-Y	630	170	31	1.7	17	130	52
	640		26		15		59
	650		9		5		86
	670		(-)24		3		73
	700		(-)10		5		85
Cs-Y	630	150	29	1.1	17	147	54
	640		24		9		67
	650		7		5		88
	670		(-)28		3		69
	700		(-)11		2		87

[a]Negative values of the amplitudes indicate rising components. Asterisk (*) indicates that the τ_3 time constants were fixed from the values obtained in the ps-experiments. The uncertainties associated with the τ_1 and τ_2 values are also reported.

Table 4

Host		Mesoporous Materials[a]		Zeolites		
		R-MCM41	Al-MCM41	CBV 500	CBV 300	CBV 100
Pore/Cavity diameter (Å)		35	35	~13	~13	~13
SiO_2/Al_2O_3 mole ratio		-	30	5.1	5.1	5.1
BET area (m^2/g)		1000	970	750	925	900
$NR_{loading}$ (10^{18} NR molecules/g_{Host})		1.9	2.0	2.4	2.5	2.6
Fluorescence lifetimes	**H-aggregates (τ_1/ps)**	320	310	90	76	80
	J-aggregates (τ_2/ns)	0.92	1.17	0.42	0.38	0.39
	Monomers (τ_3/ns)	2.49	2.69	1.43	1.19	1.07
ICT (fs)		350	320	185	166	206
VC (ps)		3.26	~3.5	1.30	1.47	1.56

[a] All the data relative to the mesoporous materials are shown in Ref. 52.

Figure 1

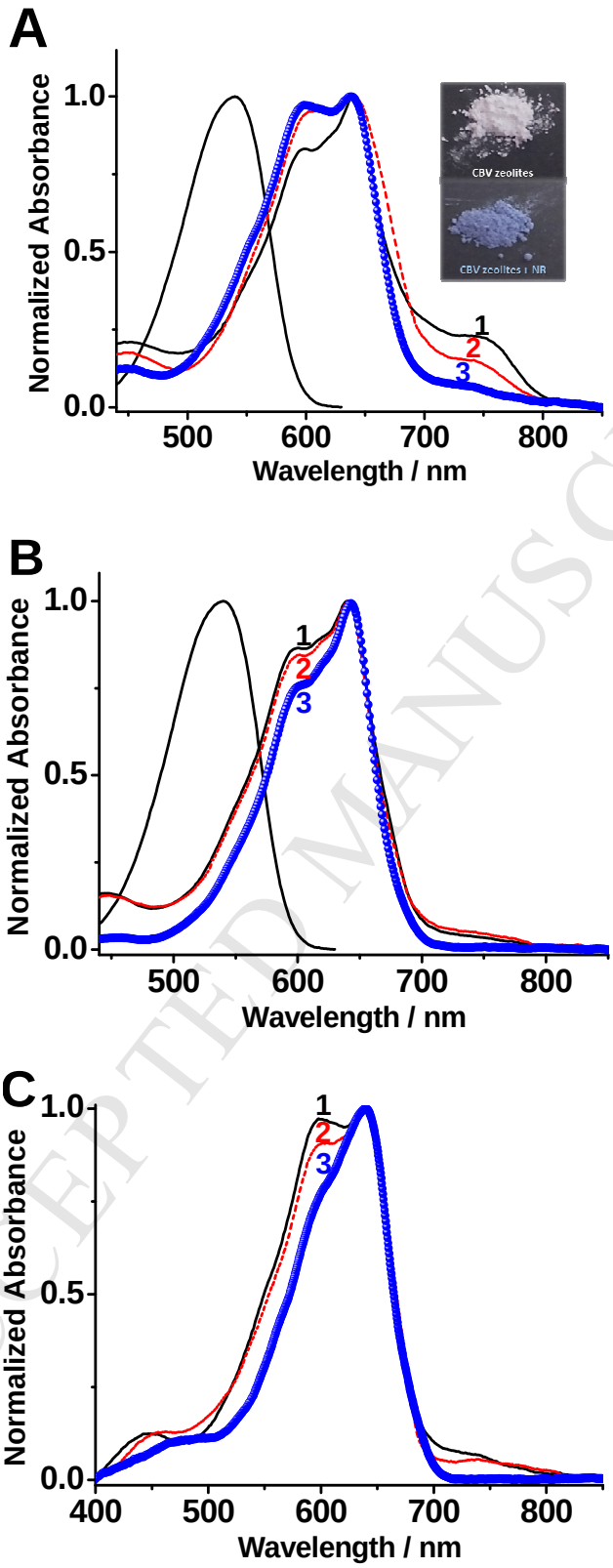

Figure 2

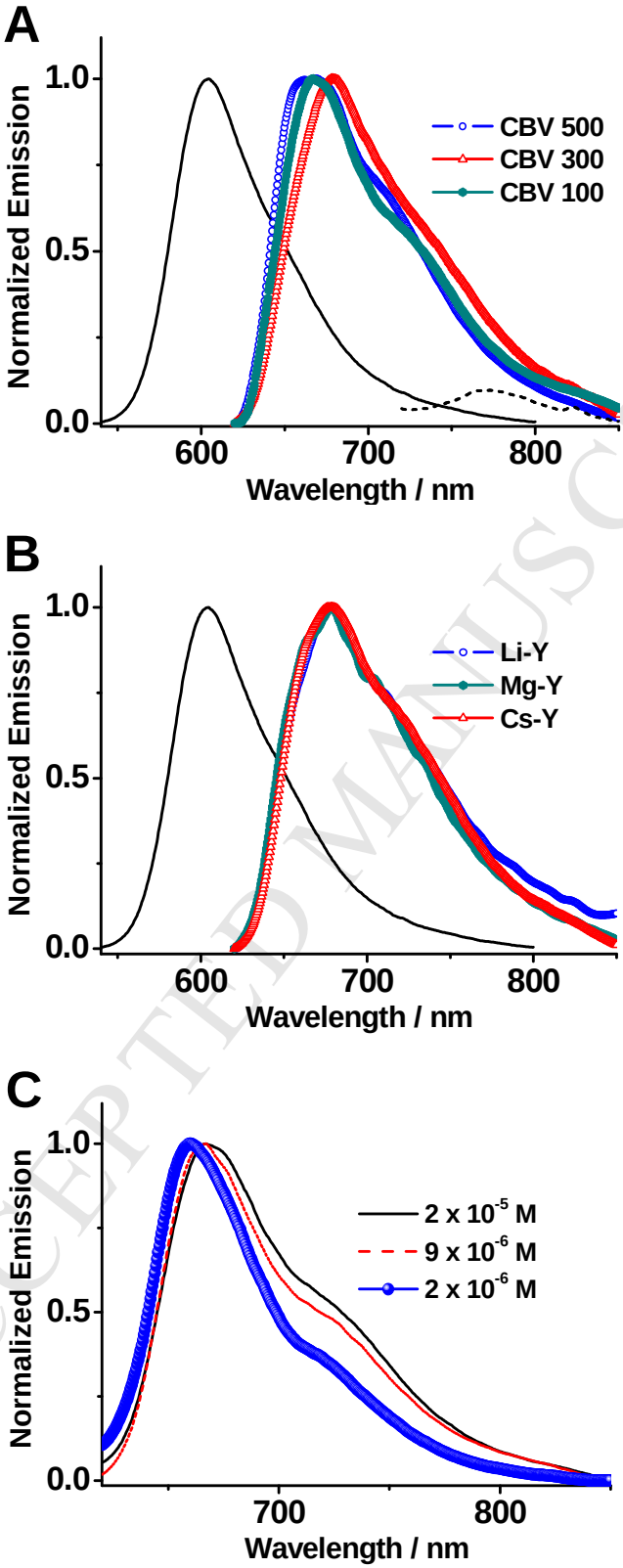

Figure 3

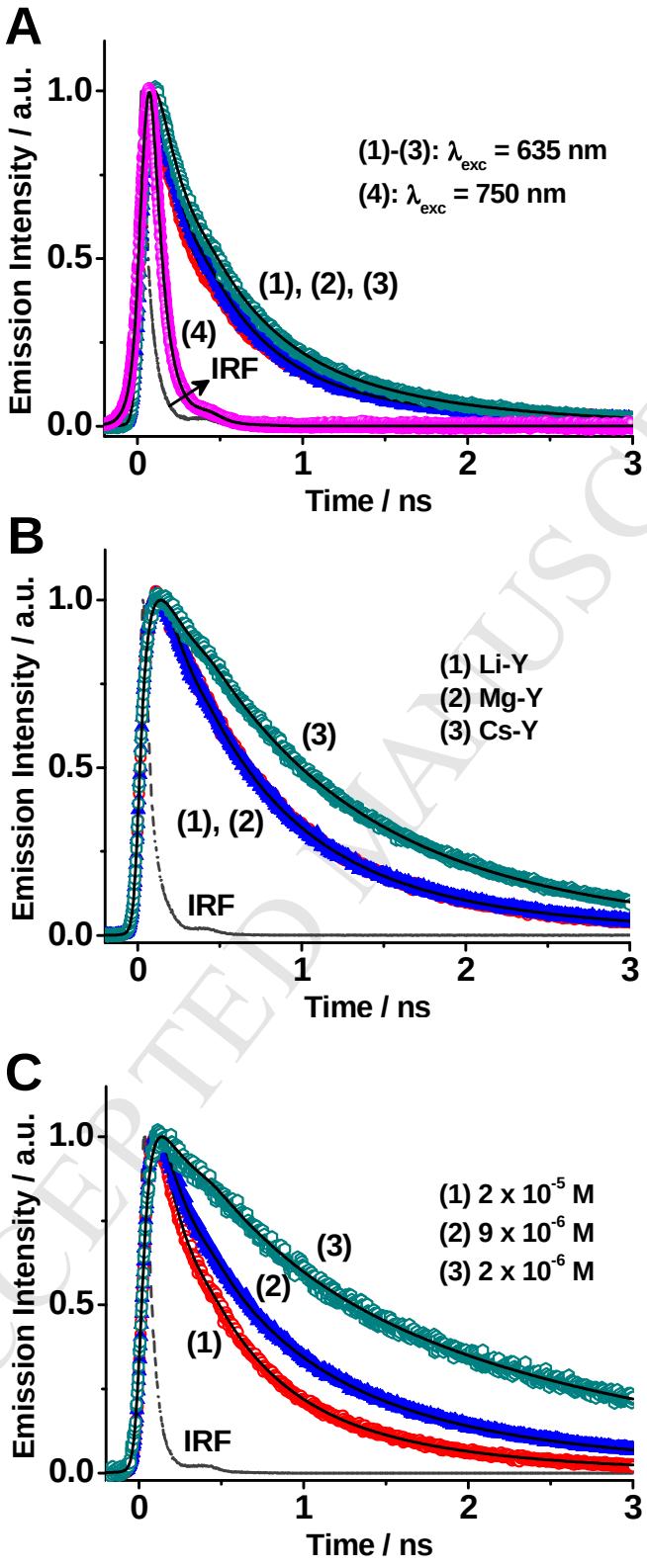

Figure 4

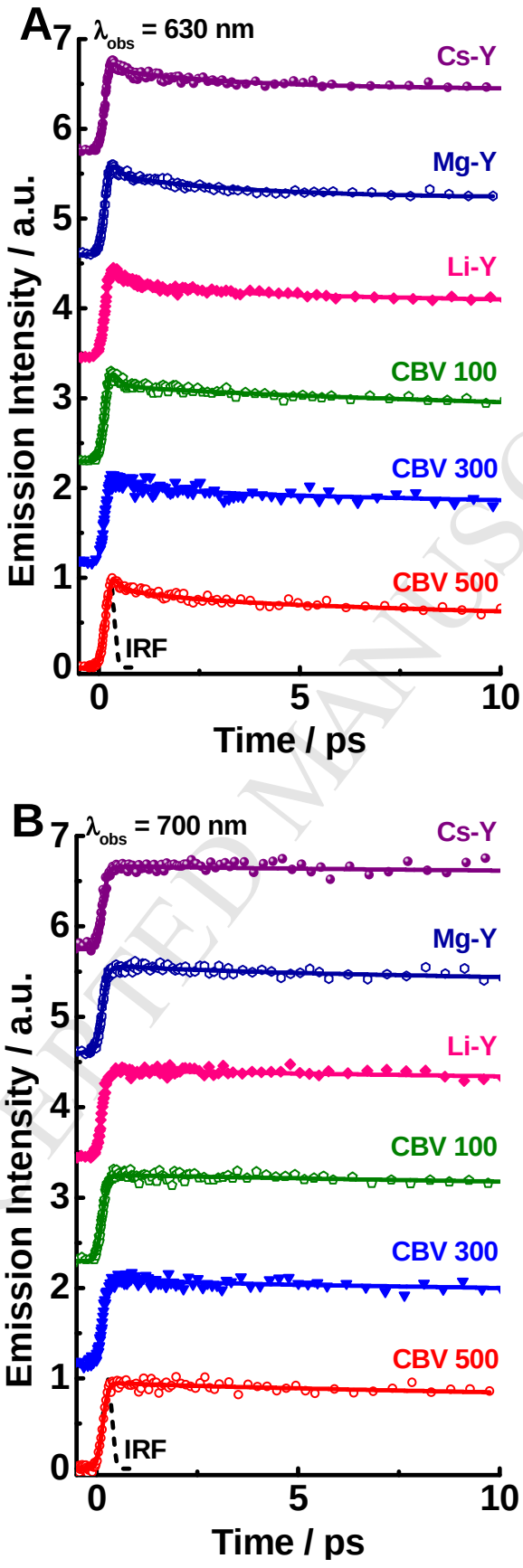

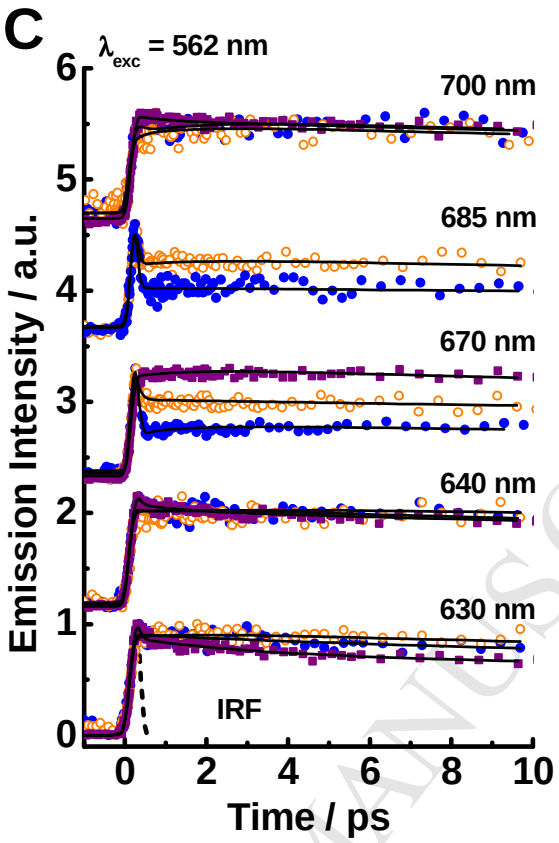

Scheme 1

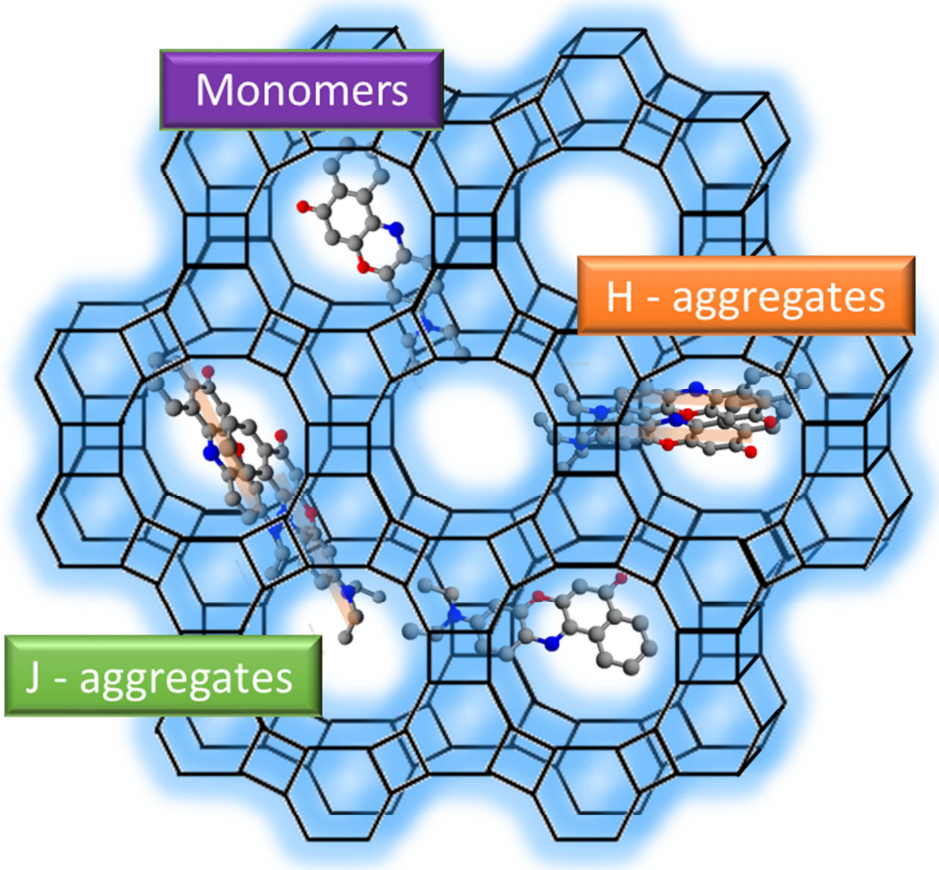

Scheme 2

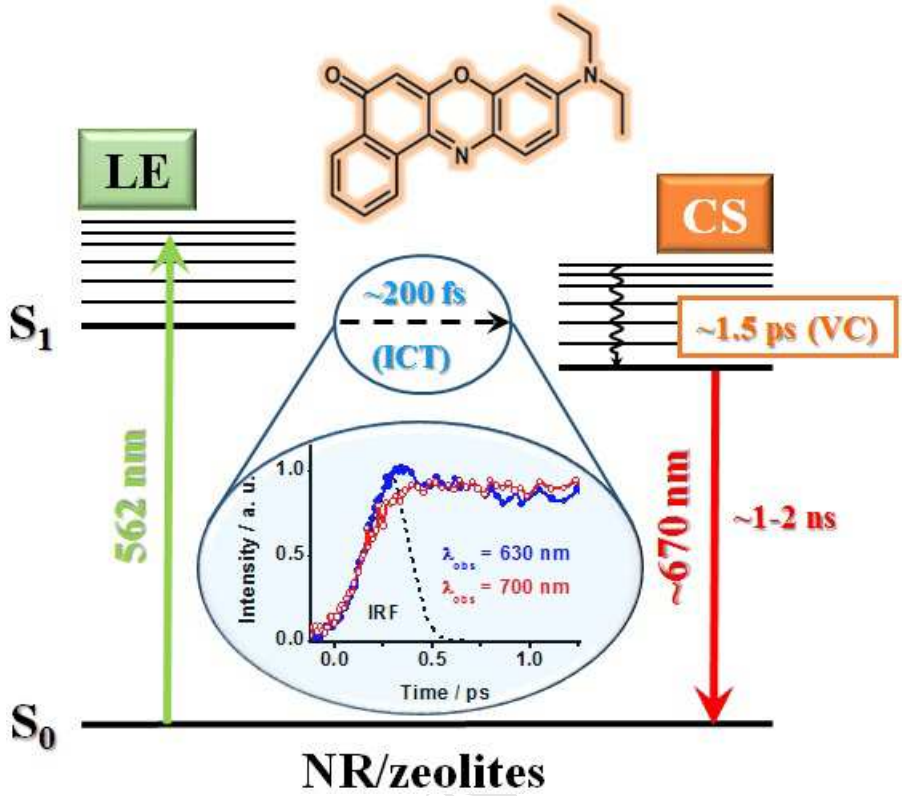

Highlights

Spectroscopic study of metal-ion exchanged zeolites using a fluorescent probe

Fast and Ultrafast-dynamics of confined molecule in metal-ion exchanged zeolites

Lewis and Brönsted acidities and the doping ion metal determine the guest dynamics